Available online at www.sciencedirect.com

jmr&t
Journal of Materials Research and Technology

journal homepage: www.elsevier.com/locate/jmrt

On the porosity-dependent permeability and conductivity of triply periodic minimal surface based porous media

Marco Sauermoser-Yri [a], *Naresh Veldurthi* [a], *Christoph Hubertus Wölfle* [b], *Preben Johnsen Svartvatn* [a], *Svenn Ove Flo Hoem* [a], *Markus Joakim Lid* [a], *Robert Bock* [c], *James W. Palko* [d], *Jan Torgersen* [b,*]

[a] *Department of Mechanical and Industrial Engineering, Norwegian University of Science and Technology, Trondheim, 7491, Norway*
[b] *Institute of Materials Science, Department of Materials Engineering, TUM School of Engineering and Design, Technical University of Munich, Garching bei München, 85748, Germany*
[c] *Federal Institute for Materials Research and Testing (BAM), Berlin, 12205, Germany*
[d] *Department of Mechanical Engineering, University of California, Merced, CA 95343, USA*

ARTICLE INFO

Article history:
Received 13 June 2023
Accepted 23 September 2023
Available online 28 September 2023

Keywords:
TPMS
Triply periodic minimal surface
Permeability
Conductivity
Porous media
Material properties

ABSTRACT

With the fast development in the field of additive manufacturing, triply periodic minimal surface (TPMS) based porous media have recently found many uses in mechanical property tuning. However, there is still a lack of understanding in their porosity-dependent permeability and electrical as well as thermal conductivity. Here, we perform finite volume simulations on the solid and void domains of the Schoen gyroid (SG), Schwarz primitive (SP) and Schwarz primitive beam (SPB) TPMS with porosities between 63% and 88% in Ansys Fluent. A simple cubic lattice (CL) of equivalent porosity served as reference. The SPB and CL showed up to one order of magnitude higher permeabilities than the SG and SP. However, SG and SP have about 1.3 and 2.6 times the electrical and thermal conductivity of SPB and CL, respectively. Furthermore, the properties of SPB and CL are largely affected by the surface area density, whereas tortuosity variation does not impact permeability and conductivity to a major extent. Finally, empirical relations are adapted to describe the presented data and thus, they may enable future designers of TPMS based porous structures to fine-tune the geometries according to the requirements on permeability and electrical as well as thermal conductivity.

1. Introduction

Triply periodic minimal surfaces, or short TPMS, are surfaces with zero mean curvature [1]. They have a three-dimensional periodicity, are found in many natural systems and are known to balance conflicting properties [1]. These surfaces may be formulated mathematically in a concise way and offer a high range of control for quantitative tuning. Their utilization in engineering structures has risen considerably with the rapid

* Corresponding author.
E-mail address: jan.torgersen@tum.de (J. Torgersen).
https://doi.org/10.1016/j.jmrt.2023.09.242

developments in the field of additive manufacturing (AM). TPMS split the space in two disjoint but intertwined regions [2]. This enables the construction of complex but highly symmetric porous structures for which the porosity may even be continuously varied in space in order to optimize the physical properties to a target application [1,3,4]. There are two ways to construct a bulk structure from a given TPMS. The first one is to assign solid material to the space between two adjacent iso-surfaces separated over a predefined distance which thus becomes the structure's wall thickness. The corresponding structures will be called *walled* TPMS. The other way is to define a single iso-surface as the boundary between the solid and void domains, which will then be called *beam type* TPMS.

To facilitate the tailoring of TPMS structures to applications, several studies on their material properties have been carried out which in particular focused on their mechanical properties. Maskery et al. manufactured various TPMS geometries with polymer additive manufacturing and investigated their mechanical properties both experimentally and with simulations [5]. Their study showed that the deformation process differed significantly between the different types of TPMS structures. Al-Ketan et al. designed and manufactured TPMS structures with functionally graded relative density, cell size and lattice type [6]. The grading direction influenced the type of deformation, e.g. loads parallel to a density grading lead to a layer-by-layer deformation. On the other hand, a load perpendicular to the grading induced a shear band like deformation. It was also shown that sheet networks for multimorphology geometries had higher elastic stiffnesses than solid networks. In another recent study on functionally graded gyroid TPMS structures Emanuelli et al. [4] investigated the influence of density gradients on the static and cyclic compressive elastic moduli of additively manufactured β-Ti21S samples. They demonstrated that these elastic properties could be tailored to those of various kinds of bone tissues for future design of implants. Lu et al. 3D printed ZnO ceramics with two different TPMS geometries and demonstrated that gyroid structures can bear more deformation till they break during compression than Schwarz primitive ones [7]. The gyroid structure was also investigated by Ma et al. , who looked at the manufacturability, mechanical behavior and permeability of these structures for use as bone scaffolds [8]. Cai et al. on the other hand explored the impact of porosity on the mechanical properties of diamond TPMS structures [9].

But not only mechanical properties were within the scope of previous investigations. Jung and Torquato [2] studied the permeability of the Schwartz primitive and diamond TPMS structures at 50% porosity as early as in 2005. They showed that the permeability is inversely proportional to the specific surfaces of the porous media. Another study on the permeability of various TPMS and strut-based porous structures was conducted by du Plessis et al. [10], who identified the gyroid to have favorable permeability among the studied TPMS geometries but noted that no simple relationship of permeability to median pore size can be obtained across all structures. Cheng et al. computationally investigated the convective heat transfer coefficient of four TPMS structures as a function of the porosity besides comparing the mechanical properties determined by experiments and theoretical analysis [11]. The heat transfer coefficient varied between the best and worst-performing structures by a factor of up to 1.9 due to differences in flow resistances [11]. The use of TPMS geometries as skeletons for a thermal energy storage system called metal foam phase change material composite (MFPCM) was analyzed by Qureshi et al. [12]. Steady-state simulations were conducted to assess the effective thermal conductivity of these skeletons, showing a reduction in melting time of 31% for the Schoen gyroid and 35.3% for the Schwarz primitive structure compared to the standard MFPCM [12]. The thermal conductivity as a function of the volume fraction of TPMS lattice structures manufactured via laser powder bed fusion was also experimentally investigated by Cathpole-Smith et al. [13]. Results indicated that the Schwarz primitive structures achieved higher thermal conductivities than the diamond and Schoen gyroid ones [13]. Niblett et al. explored the use of cubic and hexagonal lattice structures as gas diffusion layers for proton exchange membrane fuel cells [14]. They compared them computationally against the industry standard in terms of water permeability and electrical conductivity, showing improved effective electrical conductivity and two-phase transport properties [14].

Most of the studies were limited to one or two TPMS geometries, and/or only a limited range of porosities was investigated. Furthermore, thermal and electrical properties of the structures are still largely unexplored or poorly understood [5]. Therefore, one of the objectives of this work is to give fundamental insights into the various porosity-dependent material properties of three different TPMS geometries, namely the Schoen gyroid, the Schwarz primitive and the Schwarz primitive beam, to simplify the property tailoring process of such geometries. The second objective is to present an intuitive computational workflow to enable not only replication of the considered TPMS but also adaption to the study of other structures and properties. A focus will be made on the meshing procedures and mesh convergence studies of the structures as these are often not sufficiently well-described in literature. The material parameters under investigation are on the one hand, the permeability through the pore space and on the other, the electrical and thermal conductivity in the solid material of the structures. An important application where these properties matter are gas diffusion layers for fuel cells, where high permeability of the reactant fluids to the catalyst layer through the pores is desirable while the scaffold structure ideally exhibits high electrical and thermal conductivity to maximize the cell's power output and conduct excess heat away from the reaction zone, respectively. Motivated by such applications, this work investigates these properties for various TPMS structures and compares them to those of a standard cubic lattice for reference. To achieve this objective, 3D simulations of the TPMS geometries and the cubic lattice will be conducted in Ansys Fluent, both on the solid and void volume. Analytical regression models for calculating and possibly extrapolating the properties of interest will be discussed as these can simplify the design of TPMS structures. The results will be presented in a normalized fashion independent of the bulk material. Finally, a comparison to the literature is made and the general applicability of our outcomes is discussed.

2. Theory

2.1. Triply periodic minimal surfaces

In this study, the following three types of TPMS are used to generate structures for further analysis and comparison to a cubic lattice (CL): The Schoen gyroid (SG), the Schwarz primitive or Schwarz P (SP) and the Schwarz primitive Beam or Schwarz P Beam (SPB). The implicit equations to set up each of these TPMS are collected in Table 1. In this study, the terms SG, SP or SPB always refer to the 3D structures created from these respective surfaces.

The local smoothness of the curvatures is beneficial for mechanical properties and fluid transport due to lower stress concentrations and pressure drops in contrast to sharp geometries [15]. Some TPMS structures, such as the Schoen gyroid (SG) and Schwarz P (SP), are bicontinuous, meaning that the surface divides space into two disjoint but intertwining phases that are also continuous. This phenomenon is rare in two dimensions, and thus virtually unique to three dimensions which motivates the exploration of novel structures [16,17]. Bicontinuous designs are particularly useful when optimizing conflicting properties of a structure [17]. It should be noted that porosity in this work is taken as the *total* void volume divided by the total volume, so that the *sum* of the two void volumes defines porosity in case of the two considered bicontinuous TPMS.

2.2. Material parameters of the porous structures

The material parameters of interest in this study are the permeability as well as the electrical and thermal conductivity. To evaluate the permeability based on the CFD simulation results, Darcy's law is considered [14],

$$v_i = -\frac{1}{\mu} K_{ij} p_j \tag{1}$$

where Einstein summation notation is used and v_i is the fluid velocity in $\mathrm{m\,s^{-1}}$, K_{ij} is the permeability tensor in $\mathrm{m^2}$, μ is the (dynamic) viscosity of the fluid in Pa s and $p_{,j}$ is the pressure gradient in $\mathrm{Pa\,m^{-1}}$. Restricting Eq. (1) onto the normal direction n_i from the inlet surface to the outlet surface of the simulation unit cell, the effective permeability K_{eff} in $\mathrm{m^2}$, which is the permeability only in flow direction, may be written as

Table 1 – Implicit functions for the (approximate) representation of the considered TPMS [1]. $C_i = \cos(ik)$ and $S_i = \sin(ik)$, where i denotes the x, y or z coordinates, $k = \frac{2\pi}{a}$ and a is the unit cell size. The iso-parameter c may be adjusted to define the bounding surfaces and thus the wall thicknesses of the structures' solid domains.

TPMS	generating function $f_s(x, y, z) = \text{const.}$
SG	$S_xC_y + S_zC_x + S_yC_z = \pm c$
SP	$C_x + C_y + C_z = \pm c$
SPB	$C_x + C_y + C_z = c$

$$K_{\mathrm{eff}} = -\mu \frac{v_i n_i}{p_{,j} n_j} = -\frac{v\mu}{\Delta p} L \tag{2}$$

where $v = v_i n_i$ is the velocity in the inlet-outlet-direction n_i, Δp is the pressure difference between the inlet and outlet and L is the length of the simulation domain along n_i.

An equation for the effective electrical conductivity may be deduced by considering Ohm's law and the resistance R (in Ω) of an imaginary surrogate conductor of length L (in m), uniform cross section A (in $\mathrm{m^2}$) and electrical conductivity σ_{eff} (in $\mathrm{S\,m^{-1}}$),

$$R = \sigma_{\mathrm{eff}} \frac{L}{A} \qquad \text{and} \qquad U = RI \tag{3}$$

Combining these formulae and taking L and A as the length and cross-sectional area of the TPMS structure simulation cell respectively, as well as $U = \Delta\varphi$ as the electric potential difference between the inlet and outlet of the structure, we arrive at

$$\sigma_{\mathrm{eff}} = \frac{iL}{\Delta\varphi} \tag{4}$$

where $i = IA^{-1}$ is the current density in $\mathrm{A\,m^{-2}}$.

The thermal conductivity is derived similarly based on Fourier's law of heat conduction:

$$q_i = -kT_{,i} \tag{5}$$

where q_i is the heat flux density in $\mathrm{W\,m^{-2}}$, k is the thermal conductivity in $\mathrm{W\,m^{-1}\,K^{-1}}$ and $T_{,i}$ is the temperature gradient in the structure in $\mathrm{K\,m^{-1}}$. Assuming constant temperatures at the inlet and outlet and denoting the associated temperature difference as ΔT, we can use Fourier's law to obtain the effective thermal conductivity of the structure by projecting Eq. (5) onto the direction n_i from the inlet to the outlet, which yields:

$$q = q_i n_i = -kT_{,i} n_i = -k \frac{\Delta T}{L} \tag{6}$$

Thus, the effective thermal conductivity k_{eff} is given as:

$$k_{\mathrm{eff}} = -\frac{qL}{\Delta T} \tag{7}$$

For a better comparison of the electrical and thermal conductivities of the different structures, the effective conductivity ratios σ_r and k_r are introduced:

$$\sigma_r = \frac{\sigma_{\mathrm{eff}}}{\sigma_b} \tag{8}$$

$$k_r = \frac{k_{\mathrm{eff}}}{k_b} \tag{9}$$

where σ_b and k_b are the bulk conductivities of the solid volume (see Table 4).

2.3. Tortuosity

The tortuosity can be defined in several ways, either as a geometric quantity or tied to a certain property such as

Table 2 – Parameters of the modeled geometries. a is the unit cell size within the structure. The definition of T depends on the type of the structure. For the CL structures, T is the diameter of the struts. For the SG structures, T is the wall thickness. For the SP structures, T is the wall thickness in one direction (i.e. half the actual wall thickness). For the SPB structures, T is the approximate bias length used in nTopology. This parameter essentially shifts the outer wall of the structure inward or outward to set the solid and void volume ratio. L is the overall edge size of the simulation cells and ϵ is the porosity.

geometry	a [μm]	T [μm]	L [μm]	ϵ [%]
CL66	21	9	84	67.60
CL79	27	9	100	78.90
CL81	29	9	116	81.40
CL84	32	9	128	84.40
CL88	37	9	148	88.00
SG66	21	3.76	84	65.24
SG73	25	3.47	100	73.14
SG81	29	2.87	116	80.87
SG85	33	2.49	132	85.40
SG88	37	2.35	148	87.74
SP66	21	2.15	84	63.00
SP73	25	1.97	100	72.98
SP81	29	1.615	116	80.40
SP85	33	1.42	132	85.22
SP88	37	1.34	148	87.50
SPB66	21	−1.00	84	66.32
SPB68	23	−1.20	92	67.89
SPB71	24	−1.47	92	71.03
SPB73	25	−1.67	100	72.94
SPB75	26	−1.89	104	74.97

hydraulic, diffusive or electrical properties [18] in a transport process. For a fluid flowing through a porous media, the hydraulic tortuosity is commonly used. One of the definitions of the hydraulic tortuosity τ_h according to Sobieski et al. [19] is as follows:

$$\tau_h = \frac{\sum \sqrt{v_i v_i}}{\sum v_i n_i} \tag{10}$$

where $\sqrt{v_i v_i}$ is the magnitude of the velocity field in the simulated structure, $v_i n_i$ is the velocity in the direction n_i from the inlet to the outlet and the summation is carried out over all finite volumes in the pore space.

For the flow of electric charge we consider the tortuosity defined as follows:

$$\tau_e = \frac{\langle L_e \rangle}{L_s} \tag{11}$$

where $\langle L_e \rangle$ may be interpreted as the average length of the path the electrons take through the solid domain of the structure and $L_s = L$ is the length of a straight path through the solid structure, i.e. the structure's extent from the inlet to the outlet. Thus, the electrical tortuosity may be evaluated based on an electrical conductivity simulation by analyzing the resulting streamlines using Ansys' CFD-post software. An equivalent definition can be made for the tortuosity of the heat transfer in the solid domain.

Comparing the three tortuosities at hand, the main difference is that inertia plays an important role for the hydraulic tortuosity. On the other hand, electric current or heat will flow along the shortest possible way without any form of inertia, so that the associated tortuosities will differ from the hydraulic one for the same structure. The procedure on how to calculate the tortuosities in Ansys' CFD-post software is presented in Section 3.5.

3. Methodology

In this section, the workflow for modeling the TPMS geometries and generating the meshes is described.[1]

3.1. 3D model generation

One of the most integral and critical parts of simulation studies is the discretization of the geometry with finite volumes or elements with sufficient mesh quality to allow the accurate solution of the studied boundary value problem to obtain the quantities of interest. The workflow described here is similar to the ones presented by Jia et al. [20] and Feng et al. [21]. Both employed Altair HyperMesh for the meshing of the STL geometries and Dassault Systèmes Simulia Abaqus for the finite element analysis. We give a detailed description of our workflow to make it easy to reproduce the presented results. As the first step, the 3D models need to be created. The workflow for their creation in nTopology can be briefly summarized as follows (the list item index corresponds to the annotated numbers in Fig. 2 of the supplementary, where the corresponding setup steps in nTopology are shown):

1. The general model domain is created with the help of a solid cube.
2. A walled TPMS structure or the walled cubic lattice structure is created within the model domain. This represents the solid volume of the 3D structure.

[1] A slightly different workflow was used for the CL/SP geometries than the one for SG/SPB shown in the following, as the former structures were preprocessed before an updated release of the nTopology software was rolled out. Additional information on the equivalence of both workflows can be found in the supplementary.

3. A boolean subtraction is performed to create the void volume of the 3D structure.
4. A surface mesh from the implicit body is created via a triangle tessellation.
5. The geometry is exported as an STL file.

The STL files were then exported to Ansys SpaceClaim [22] after undergoing a quality check, ensuring there are no self-intersections or other defects like hanging nodes. Ansys SpaceClaim was found to be adequate for handling large sizes of tessellated files and furthermore provides the option to define boundaries on the TPMS structures.

These steps were repeated for each structure and porosity. Table 2 gives an overview of the relevant geometrical parameters of the modeled TPMS and cubic lattice structures. The name for each structure was chosen to be a combination of the geometry type and porosity value, e.g., SG73 represents a Schoen gyroid geometry with a porosity of approximately 73%.

In general, porosities ϵ were varied between 63% and 88%. Lower porosities were not investigated as these lead to either converging effective properties or diminishing differences of these between the various structures. A smaller porosity range (up to 78.6%) was investigated for the SPB structures. The reason for this upper limit is that at higher porosities the SPB structure becomes discontinuous due to disconnection of the struts. On the other hand, TPMS structures have a minimum porosity as well in transport layer applications below which the pores become disconnected and the structure can consequently not be used for fluid transport. The minimum porosity for the SG structure is approximately 9%, for the SP structure approximately 44% and for the SPB structure approximately 22%. The limit porosities were explored by varying the geometries in nTopology until disconnection of the void or solid spaces occurred. Fig. 1 shows visualizations for some of the different geometries exported to Ansys SpaceClaim.

3.2. *Meshing*

The TPMS structures and the cubic lattice were studied using Ansys Fluent 2021 R1. To this end, the generated structures

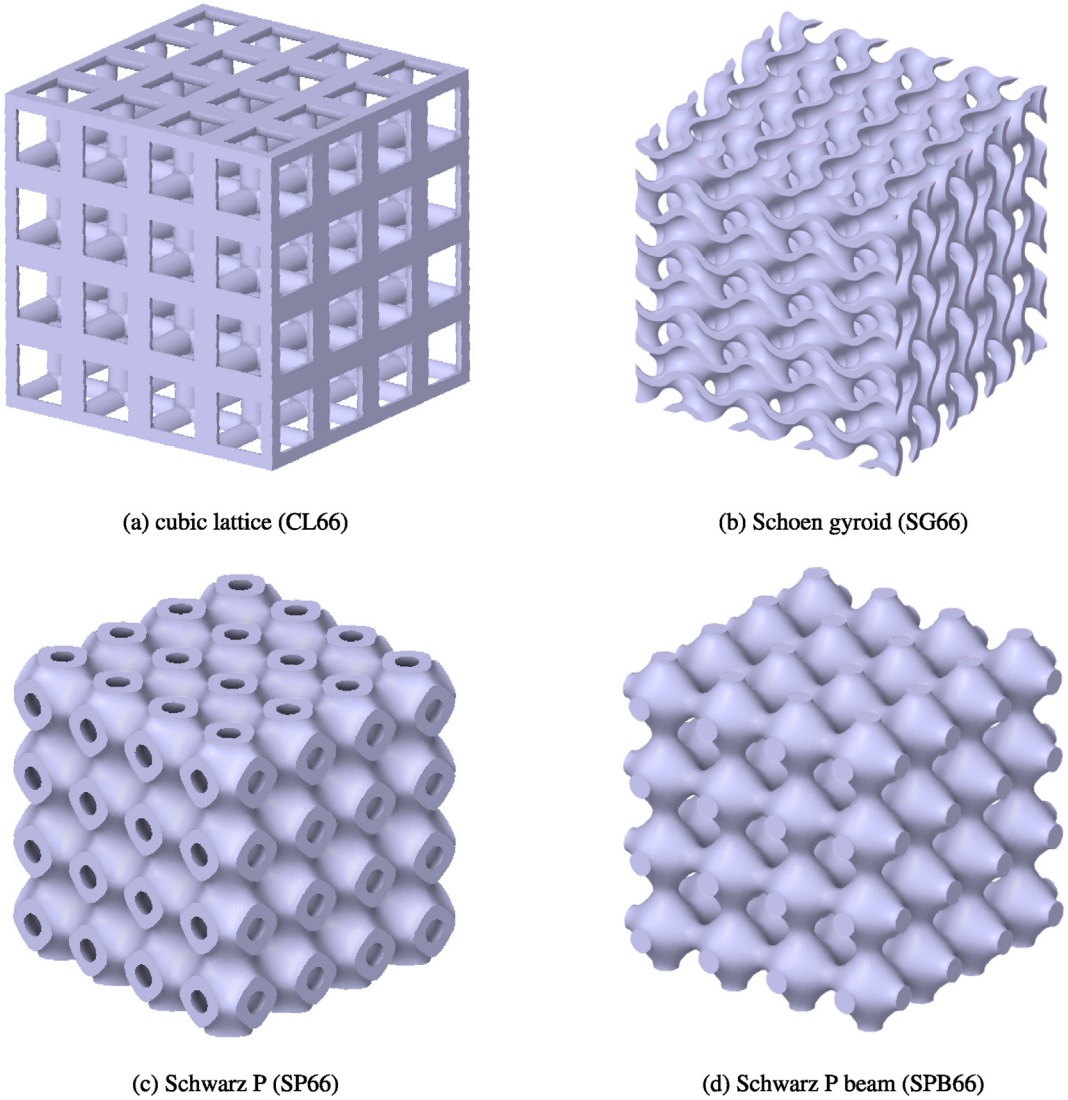

(a) cubic lattice (CL66)

(b) Schoen gyroid (SG66)

(c) Schwarz P (SP66)

(d) Schwarz P beam (SPB66)

Fig. 1 – Examples for each type of the studied structures.

were imported as SpaceClaim files (.scdoc) into Ansys Fluent for meshing (see Fig. 1 for examples of the geometries). The meshing was done using conventional bottom-up procedures, creating a surface mesh followed by a volume mesh.

For the surface meshing, the mesh control options in Ansys Fluent provide local sizing controls like curvature and proximity size functions for mapping and meshing the curvature surfaces and faces/edges of the geometries. Dense surface mesh elements on the TPMS structure's curvatures, such as the SG structure, were created by using a curvature normal angle of 18°, which divides the geometry curvature arc by 18°. The proximity size function establishes the meshing between the gaps of the selected edges and faces in the domain. Thus, the surface meshes could be tailored with adequate cell size and quality by using such sizing functions. Building high-quality surface meshes facilitates an efficient generation of smooth volume meshes for the TPMS structures. The volume meshes of the SG and SPB structures were composed of polyhedral elements, while the CL and SP structures were meshed using tetrahedral elements, ref. to the supplementary for further information. In both cases, a conformal mapping technique was applied after the volume meshing. The boundary layers were projected on the walls of the CL and the considered TPMS structures. Five inflation or boundary layers were meshed with a growth factor of 1.2. The solid volumes of the TPMS geometries were systematically varied and meshed in the same fashion as the void volume. The elements of the discretized structures were constrained to conform to skewness, orthogonality and aspect ratio within set in ranges. These quality criteria significantly enhanced the simulation robustness w.r.t. convergence of the approximate solution.

3.3. Governing equations and solution methodology

The numerical simulations in Ansys Fluent [23] iteratively solve a set of governing equations that follow from conservation laws in order to compute the flow within the meshed geometries. For the computation of the permeabilities, steady-state and incompressibility assumptions were made for the fluid flow. These simplify the continuity and the Navier–Stokes equations as follows:

$$v_{i,i} = 0 \tag{12}$$

$$-\mu v_{i,jj} + \rho_w v_j v_{i,j} + p_{,i} = F_i \tag{13}$$

here, cartesian coordinates are assumed and v_i is the velocity, ρ_w the density of water, $p_{,i}$ the pressure gradient, μ the dynamic viscosity of the fluid and F_i denotes the external forces. The energy equation was not considered as heat transfer and temperature changes were disregarded in the fluid. The permeability calculations involving Darcy's law require a low Reynolds regime which is satisfied by the steady-state, incompressible and very low velocity ($<10e-6\,ms^{-1}$) flows at hand. Furthermore, in the simulations done in this work, the convective/inertial and gravitational forces in the Navier-Stokes equation were overwhelmingly small.

The governing equation for the linear, isotropic electrical conduction is:

$$(\sigma\varphi_{,i})_{,i} + S = 0 \tag{14}$$

here, φ is the electric potential, σ the electrical conductivity of the solid material and S a source term, which is zero for the purpose of our study.

For the thermal analysis of the solid domain, the conventional heat conduction equation is used, which has the same mathematical structure as Eq. (14):

$$(kT_{,i})_{,i} + S_h = 0 \tag{15}$$

in this equation, k is the thermal conductivity, $T_{,i}$ the temperature gradient and S_h a heat source term, which is zero for our purposes as we assume that there are no internal sources of heat (e.g. Joule heating).

The electrical and thermal simulations were run on the solid domains of the geometries under steady-state assumptions, where the potential module was enabled in Ansys Fluent. Thus, the electrical and heat conduction problems could be solved simultaneously. In the Ansys Fluent simulations, the solution methodology involved employing the SIMPLE algorithm to solve the discussed governing equations [23]. The chosen segregated algorithm worked well with the adoption of second-order upwind schemes to evaluate pressure and momentum equations and the iterative solver converged to a solution of the continuity and momentum equations within the set convergence criteria (1e−10).

Based on the computed fields, the permeability as well as the effective electrical and thermal conductivities of the CL and TPMS structures were extracted as detailed in section 2. To calculate the effective permeability K_{eff} with Eq. (2), the volume-averaged velocity perpendicular to the inlet and outlet plane was calculated with the built-in report tools of Ansys Fluent. For the effective electrical conductivity σ_{eff} (Eq. (4)), the area-averaged electric current magnitude was calculated at the inlet and divided by the calculated inlet area to receive the current density i. The effective thermal conductivity k_{eff} was computed based on Eq. (7) and by using the flux report tool in Ansys Fluent to calculate the effective heat flux q.

3.4. Boundary conditions and assumptions

To evaluate the permeability, the electrical and the thermal conductivity via simulations, boundary conditions and further assumptions are required. In the permeability analysis, the pressure difference between the inlet and outlet drives the fluid through the structures' pore spaces. The corresponding boundary conditions for the inlet and outlet surfaces and the external and internal walls (i.e. the outer walls of the simulation cell and the internal boundary of the solid volume, respectively) are tabulated in Table 3. The low pressure difference was prescribed in consideration of the simulation cell dimensions and the practical applicability. However, the magnitude of the pressure drop does not influence the effective permeability since the latter is a structural property [24]. The no-slip condition was set on the internal walls of the geometries, where the fluid-wall interactions are vital because of the dominance of viscous forces in laminar flows [25, 26]. The symmetry boundary condition on the external walls reduced the computational time needed to simulate the properties of large porous media. Note that periodicity is

Table 3 – Boundary conditions for the three types of simulations used for all geometries.

simulation	inlet	outlet	external walls	internal walls
Permeability	0.01 Pa	0 Pa	symmetry	no-slip
Electrical conduction	1 V	0 V	symmetry	$i = 0$
Thermal conduction	305 K	300 K	symmetry	$q = 0$

expected for the field solutions and periodic boundary conditions on the simulation cell walls perpendicular to the principal flow direction would constitute a natural way of modeling this. However, for reasons of technical simplicity in our particular model generation pipeline and robustness of the CFD simulations, we use symmetry boundary conditions but consider an aggregate of $4 \times 4 \times 4$ TPMS unit cells as our simulation cell to alleviate the influence of this boundary condition. A more detailed account of this aspect and the suitability of these specific boundary conditions can be found in the supplementary material. The boundary conditions for the electrical and thermal simulations on the solid geometries are also tabulated in Table 3. For the electric/thermal simulation, the prescribed potential/temperature difference across the inlet and outlet drives the current/heat flow in the solid domains of the geometries. Here, the conditions $i = 0$ and $q = 0$ for the normal fluxes on the internal walls imply that the electric/thermal conductivity is zero, i.e. the walls are electrically/thermally insulated.

The fluid and the material of the solid domain to be modeled were water and glassy carbon (GC), respectively. Table 4 lists the relevant properties of both. GC was chosen as it is promising especially for micro and nano applications and can be obtained by heat treating certain polymers [27]. Furthermore, GC was chosen to obtain results comparable to the study of Niblett et al. [14].

3.5. Computing the tortuosities

To evaluate the hydraulic tortuosity τ_h, the following procedures are followed along Eq. (10).

- $\sum \sqrt{v_i v_i}$ is calculated using the volume integral and sum function in Ansys Fluent, applied to the whole pore space of the geometry. Afterwards, the velocity magnitude is reported.
- $\sum v_i n_i$ is computed using again the volume integral and sum function of Ansys Fluent for the pore space followed by extracting the velocity in flow direction.

The electrical tortuosity τ_e is computed in the CFD-post software of Ansys Fluent based on the streamlines of the solution field. Let N be the number of the considered streamlines γ_i (where $i = 1 \ldots N$) connecting inlet and outlet, which may be thought of as smooth curves in the simulation domain with some parametrization $\gamma_i : [0, l_i] \mapsto \mathbb{R}^3$. The length L_{γ_i} of the streamline γ_i is then given by the line integral $L_{\gamma_i} = \int_0^{l_i} \|\gamma_i'(s)\|_2 ds$ (with $\|\bullet\|_2$ denoting the euclidean norm) and the tortuosity may be taken as the ratio of the average lengths of the streamlines and the length of the straight path, i.e. the edge length L of the simulation cell:

$$\tau_e = \frac{\langle L_e \rangle}{L} \approx \frac{1}{L} \frac{1}{N} \sum_{i=1}^{N} L_{\gamma_i} \tag{16}$$

The number of streamlines was chosen by conducting a convergence study where N was increased until the tortuosity τ_e converged. The thermal tortuosity can be handled in the same way.

Table 4 – Material parameters of water and glassy carbon (GC) for the simulations [28,29].

Property	Value	Unit
Water density ρ_w	998	$kg\,m^{-3}$
Water viscosity μ	1e-3	$Pa\,s$
GC density ρ_{GC}	1.4	$g\,cm^{-3}$
GC resistivity ρ	4e-6	$\Omega\,m$
GC bulk electrical conductivity σ_b	2.5e5	$S\,m^{-1}$
GC bulk thermal conductivity k_b	6.3	$W\,m^{-1}\,K^{-1}$
GC specific heat capacity c_p	862.3	$J\,K^{-1}\,kg^{-1}$

3.6. Mesh convergence study

Mesh convergence studies for TPMS and CL geometries were performed. The boundary conditions used in the Ansys Fluent simulations are discussed along the results of this convergence study. In the supplementary, Tables 5 and 6 show the computed permeability and electrical conductivity (or inverse inlet potential) as an indicator quantity of convergence in relation to the mesh element count.

The permeability simulations involve solid-fluid interactions for which the boundary layers along the solid walls were carefully set up to resolve the variation of the velocity gradients and shear stresses near the walls given the prescribed no-slip boundary conditions. In laminar flows, the viscous forces have predominance as influence for the velocity gradients and thus, Darcy's velocity decreases with an increase in viscous forces. For the CL geometry with 68% porosity, as shown in Supplementary Table 5, the permeability did not vary considerably after surpassing 2.13 million mesh elements, and for the SG geometry with 66% porosity, this was the case for approximately 21.1 million mesh elements. These mesh sizes are thus adequate for our study of the CL and SG structures with varying porosities. The same holds for SP (81% porosity) and SPB (66% porosity) geometries, where approximately 16.9 and 3 million mesh elements were used, respectively.

Results for the mesh convergence study of the solid structures with respect to the electrical conductivity are tabulated in Supplementary Table 6. For the CL and SP structures, the inverse of the inlet potential φ_{in} is considered to judge mesh convergence while the electrical conductivity was considered for the SG and SPB structures.[2] The effective

[2] This difference was due to changes in the computational setup but is not critical in a mesh convergence study.

electrical conductivity is affected by the path length the electrons take. Due to the relatively straight electron paths for the CL and SPB geometries, the electrical conductivity is expected not to change significantly with increased mesh element count. For the CL geometry with 81% porosity, the effective conductivity did not vary after approximately 2.08 million mesh elements. For SPB geometry with 66% porosity, this holds for 2.81 million mesh elements, as shown in Supplementary Table 6. Similarly, for the SG and SP geometries, the effective conductivity does not vary from approximately 4.3 million mesh elements onwards with 66% and 88% porosities, respectively.

4. Results and discussion

4.1. Permeability simulations

After the simulations, the Knudsen number was investigated to see if Darcy's law applies to our systems. The Knudsen number, *Kn* was calculated as

$$\mathrm{Kn} = \frac{\lambda}{L_c} \tag{17}$$

where λ is the mean free path based on the equivalent diameter of the water molecule [30] and L_c is the smallest characteristic length of all the geometries. In this case, λ is 0.3853 nm and L_c was conservatively chosen as 5 μm which is approximately a fourth to a seventh the size of the unit cells. This resulted in a *Kn* of around 7.7e-5. For *Kn* below 0.01, a continuum model is usually applicable and Darcy's law is valid [30].

Furthermore, the Reynolds number, *Re* (Eq. (18)) was checked to confirm that the flow is within the laminar regime.

$$\mathrm{Re} = \frac{\upsilon D_p}{\nu} \tag{18}$$

where $\upsilon = 1.25 \times 10^{-6}$ ms^{-1} is the maximum of the average velocities found in all simulations, $\nu = 1 \times 10^{-6}$ m^2 s^{-1} is the kinematic viscosity at room temperature and D_p is the characteristic dimension of the flow channels in the structures which was taken as the diameter of the largest circle that can be fit inside the void area of the structure. As an example, for SPB75 we found $D_p = 19$ μm and calculating the *Re* according to Eq. (18) based on this yields about 2.4e-5 which suggests laminar flow.

The effective permeability in m^2 for all simulated structures can be found in Fig. 2 as a function of the porosity ϵ.

As expected, a permeability increase can be seen if the porosity ϵ is increased due to the gain of void volume. In theory, at zero porosity, the permeability should also be zero as there is no void volume available for the flow. However, since there is a non-zero lower bound on porosity for practical purposes, we consider a fitting model with slightly different behavior at zero porosity. Specifically, an exponential model was considered, as indicated in Fig. 2. The results show that the CL and SPB structures have superior permeability compared to the SG and SP ones. At higher porosities, these differences become more significant. Overall, the most permeable structure at a given porosity is the SPB structure.

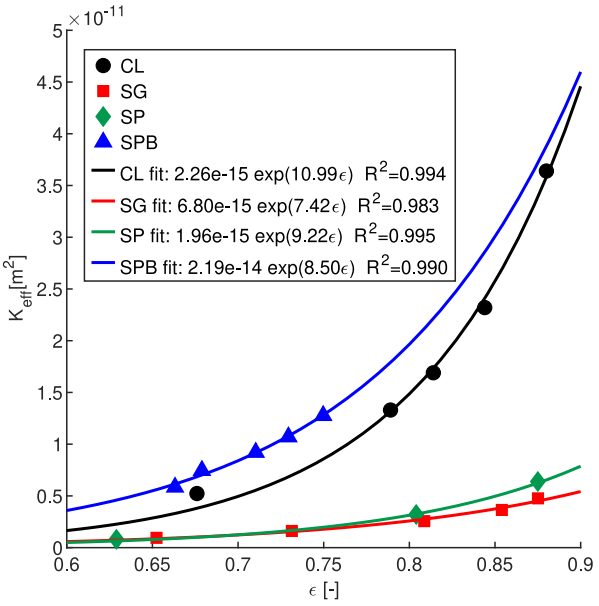

Fig. 2 – Effective permeability K_{eff} in m^2 as a function of the porosity ϵ for the different structures, including curve fit data.

However, this structure is limited to a maximum porosity of $\epsilon = 78.6\%$ as the struts disconnect for higher ϵ. Thus, for porosities above roughly 75%, the CL geometry is the most permeable realizable structure. The computed permeabilities will be compared to literature results in section 4.5.

The disparity between the CL/SPB (beam type) and the SP/SG (walled) structures can be related to their geometrical properties. The first relevant property is the surface area which influences the friction of the flowing medium. Fig. 3 shows the ratio AV_s^{-1} of the surface area *A* to the solid volume V_s, denoted as surface area density in the following, for each studied structure and porosity. Note that an equal and fixed number of TPMS/CL unit cells within the simulation domain has been considered in all studied cases. This ratio is considered instead of the absolute surface area because structures with higher porosities have a larger unit cell size (see Table 2), thus requiring a normalization of the surface area. The higher the surface area density, the more surface friction and thus resistance the fluid experiences when permeating the structure. Thus, as seen in Fig. 3, the structures with the highest permeability have the lowest surface area (however, no simple quantitative relationship could be established between the surface area density and the permeability). The fact that walled TPMS structures have considerably higher surface area densities than beam type ones was also noted by Al-Ketan et al. [31]. Another reason for the disparity of the permeabilities is the hydraulic tortuosity. The higher τ_h is for a structure, the longer the distance between the inlet and the outlet becomes for a particle of the flowing medium. This means that the friction losses increase, which thus lowers permeability. Fig. 4 shows the computed hydraulic tortuosities. The SG structures have much larger tortuosities compared to the other structures, primarily due to

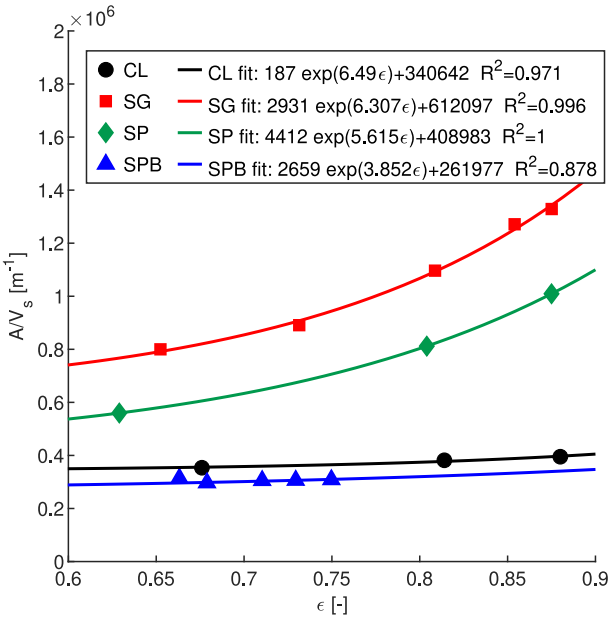

Fig. 3 – Surface area density AV_s^{-1} in m^{-1} as a function of the porosity ϵ for the studied structures (each containing an array of 4 × 4 × 4 unit cells), including curve fit data.

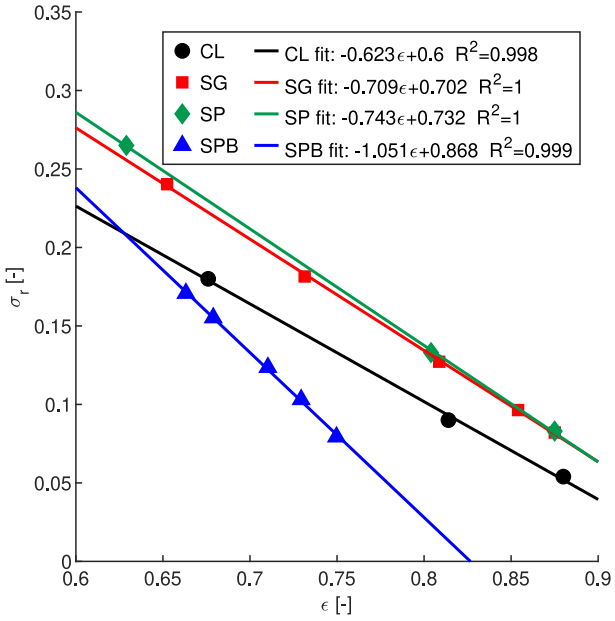

Fig. 5 – Electrical conductivity ratio σ_r as a function of the porosity ϵ for the different structures, including curve fit data.

their highly intertwined flow channel geometries. This observation agrees well with the findings of Guerreiro et al. [32]. On the other hand, even though the SP structure has τ_h values similar to the CL and SPB geometries, its permeability is much lower, indicating that the surface area density (see Fig. 3) is the decisive aspect here. This case signifies that there is a complex connection between the geometric properties of TPMS structures and their permeability.

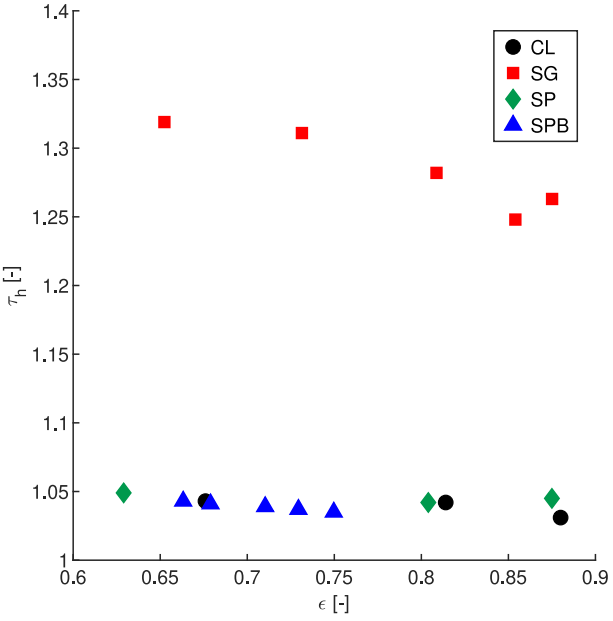

Fig. 4 – Hydraulic tortuosity τ_h as a function of the porosity ϵ for the different structures.

4.2. *Electrical conduction simulations*

Fig. 5 shows the electrical conductivity ratio σ_r (Eq. (8)) for each geometry at different porosities. The data suggests a linear dependency on porosity (ref. to the linear regression results shown in the legend of Fig. 5). A comparison to electrical conductivity results from literature is postponed to Section 4.5. As expected, the conductivity ratio generally decreases with increased porosity since there is less solid volume then for the conduction of current. Contrary to the results of the permeability simulations, the SG and SP structures are the best-performing ones in terms of electrical conductivity while the SPB is the worst in this regard. However, extrapolation to porosities lower than $\epsilon = 0.65$ suggests that the SPB structures might have higher electrical conductivity ratios than SP and SG structures in the lower porosity range.

Analyzing the current density distribution of the CL and SPB structures (Fig. 6 left shows the SPB structure), one can see the reason for the lower electrical conductivities. Due to the straighter "flow channels" for the electric current compared to SP and SG structures, there is a considerable solid volume fraction (blue areas in Fig. 6 left) which is not utilized for current transport from the inlet to the outlet, thus decreasing the conductivity ratio. This unused solid volume consists mainly of the straight beams of the structures that lie perpendicular to the current flow direction. On the other hand, nearly all the solid volume of the SP and SG geometries are used to transport current, see Fig. 6 right for an example of the SG structures.

Another influencing factor for the electric current flow (and thus conductivity) is the electrical tortuosity (Eq. (16)) which is seen in Fig. 7. The structures can be divided into two groups based on the electrical tortuosity τ_e. The walled TPMS structures (SG and SP) exhibit higher tortuosities of about 1.15. On

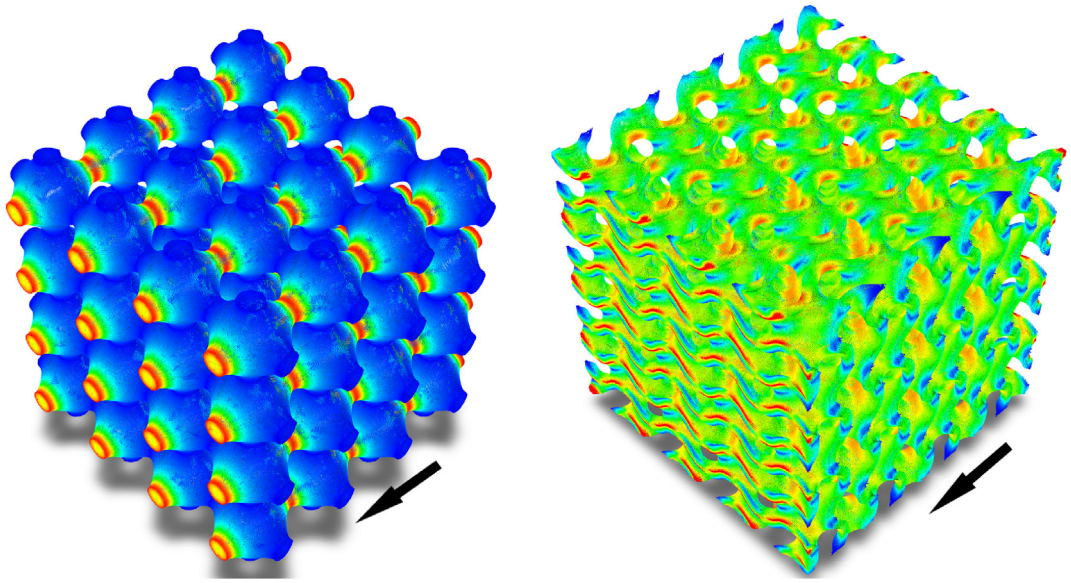

Fig. 6 – Electric current density distributions for the SPB68 structure (left) and the SG68 structure (right). Red is the highest and blue is the lowest current density. The arrows indicate the direction of the electric current flow.

the other hand, the beam type structures (SPB and CL) have a low tortuosity of 1.07 and below which means that current essentially moves along straight lines through them with the beams normal to that direction contributing, as noted before, little to the electrical conduction.

As shown in the permeability analysis, the hydraulic tortuosity of the walled SG structure is higher compared to all the other structures due to its intertwined flow channels. However, both walled TPMS structures (SG and SP) exhibited a similar electrical tortuosity. This could be explained by the (geometrical) tortuosities of the solid and void volumes, which have quite different magnitudes for the SP structure but less so for the SG structure. Furthermore, note that increased tortuosity does not necessarily have a negative impact on the effective electrical conductivity, which is demonstrated by the structures with the highest τ_e having nonetheless the highest σ_r. For example, as the SPB's electrical tortuosity is only slightly higher than for the CL structure, it is concluded that more volume is used in the former for the electrical conduction which indeed relates to the thicker minimal cross-sectional area of the SPB structure's struts compared to the CL's at equal porosity. This geometrical influence is becoming more marked for higher porosities, which may explain the steeper slope of the SPB's electrical conductivity ratio seen in Fig. 5. Further elaboration on these aspects is deferred to section 4.4.

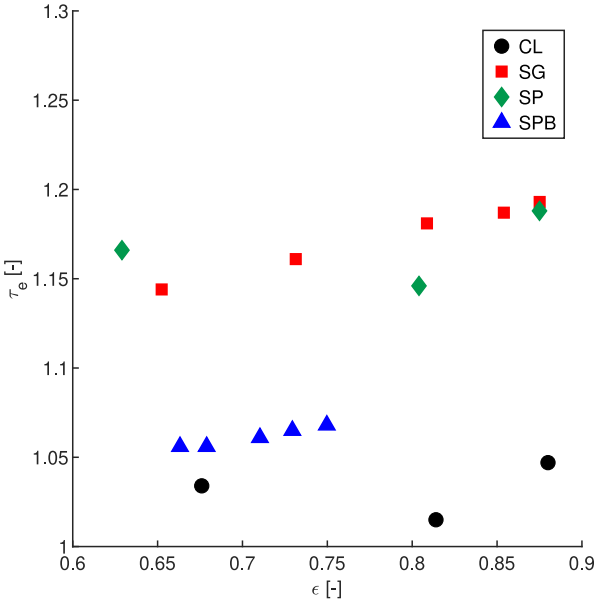

Fig. 7 – Electrical tortuosity τ_e as a function of the porosity ϵ for the different structures.

4.3. *Heat conduction simulations*

As stated before, the governing equations of the heat conduction and the electrical conduction problem have the same mathematical form – only the absolute bulk material values obtained in the solving process differ. Due to the normalization to the bulk values, the conductivity *ratios*, however, are independent of the absolute values of the simulations' input parameters and thus, thermal and electrical conductivity ratios are expected to coincide. Hence, we limit the presentation in this section to the SG and SPB structures and point to the supplementary for additional thermal simulations carried out on the other structures.

Fig. 8 shows the thermal conductivity ratios for the SG and SPB structures. A comparison with Fig. 5 confirms the expectation of equality of thermal and electrical conductivity ratios. Note that the thermal and electrical tortuosities coincide, too, as both relate to the same solid volume and essentially equivalent governing transport equations. Therefore, we will

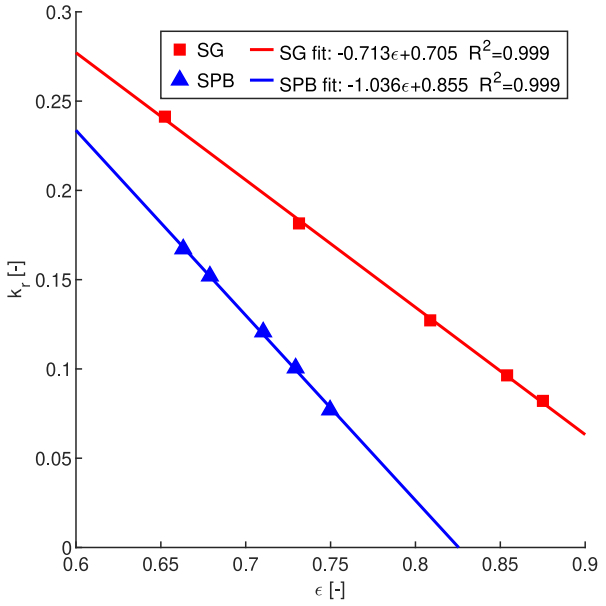

Fig. 8 – Thermal conductivity ratio k_r as a function of the porosity ϵ for the SG and SPB structures, including curve fit data.

limit the discussion to the electrical conductivity in the remaining sections of the paper.

As the thermal conductivity is an essential structure parameter, e.g. for heat exchangers, it is instructive to do some further exploration in such contexts particularly in connection with the structure's surface area density A/V_s (see Fig. 3) [13]. The influence of the geometry on the thermal conductivity may thus be investigated more intuitively, see Fig. 9, where the relation between thermal conductivity ratio k_r and surface area density A/V_s is displayed. Fig. 9 shows, similar to previous results, that the walled TPMS structures are grouped up in a different range compared to the beam type structures. An inverse relationship between increasing surface area density and thermal conductivity ratio is found. This aligns well with the experimental findings of Catchpole-Smith et al. [13]. Note that the surface area density of the beam type structures is independent of porosity so that we may not establish a useful relation to the thermal conductivity for the CL and SPB structures. In contrast, the thermal conductivity ratio of the walled TPMS structures decreases over a wider range of surface area densities.

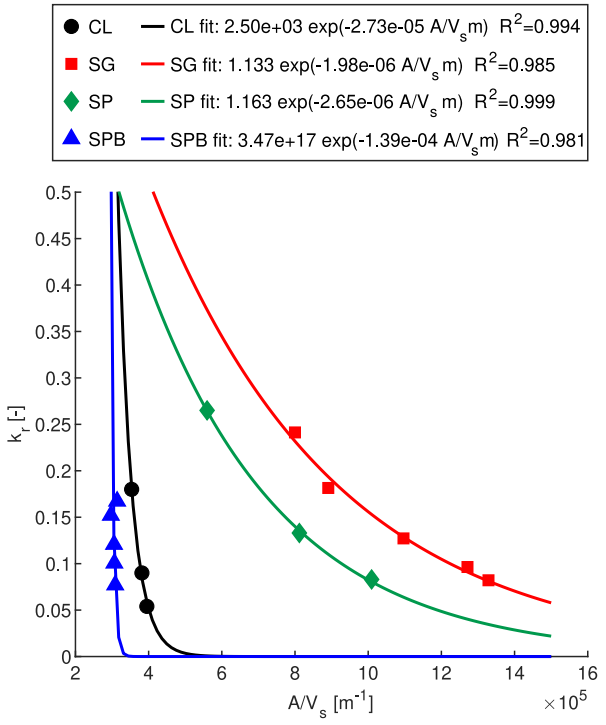

Fig. 9 – Thermal conductivity ratio k_r as a function of the surface area density A/V_s for the different structures and associated curve fit data using an exponential model function.

To expand on these observations, the thermal diffusivity D_t defined by

$$D_t = \frac{k_r k_b}{\rho_l c_p} \tag{19}$$

was calculated and plotted against the surface area density, see Fig. 10. Here, k_b is the bulk thermal conductivity, $\rho_l = \rho_b(1-\epsilon)$ is the "lattice density" with $\rho_b = \rho_{GC}$ denoting the density of the bulk material and c_p the specific heat capacity. From Fig. 10 we might conclude that the walled TPMS structures are surface area density and porosity dependent, whereas the beam type structures' heat conduction capabilities are only porosity limited.

Overall, our computations show that SG and SP structures are preferable for heat exchangers compared to SPB and CL geometries at a given porosity, which was also shown by Kaur et al. [33].

4.4. *Gibson-Ashby relationship*

In the previous sections, we have primarily discussed the structures' parameters for varying porosities. A widely considered relation for the parameters of porous structures is the Gibson-Ashby relation [34]. In this section, we shall check if it also applies to the TPMS structures at hand and their non-mechanical properties. The discussion is focused on the electrical conductivity ratios of the TPMS structures (as noted previously, the thermal conductivity ratio is identical and hence the conclusions drawn will carry over to k_r).

Fig. 11 shows the electrical conductivity ratio σ_r plotted against the density ratio $\rho_l/\rho_b = 1-\epsilon$. A Gibson-Ashby relation [34] was applied for the curve fit. This relationship fits all the structures we considered very well, as seen in Fig. 11. Note that the conductivity ratio σ_r approaches zero with $\rho_l/\rho_b \to 0$ for a Gibson-Ashby type relation, which is necessary since there is no solid material left to conduct the electrons in this limit. However, for the SPB structure, σ_r actually approaches a zero limit at higher porosities: At around 78.6% porosity ($\rho_l/\rho_b = 0.214$), the struts of the SPB structure disconnect from each other and therefore, no current or heat can be conducted. This implies that the Gibson-Ashby relation can only be applied in a meaningful way for SPB structures in a particular porosity region below 78.6%.

Another important point is that the Gibson-Ashby fits for the SG, SP and CL structures do not satisfy $\sigma_r = 1$ in the limit $\rho_l/$

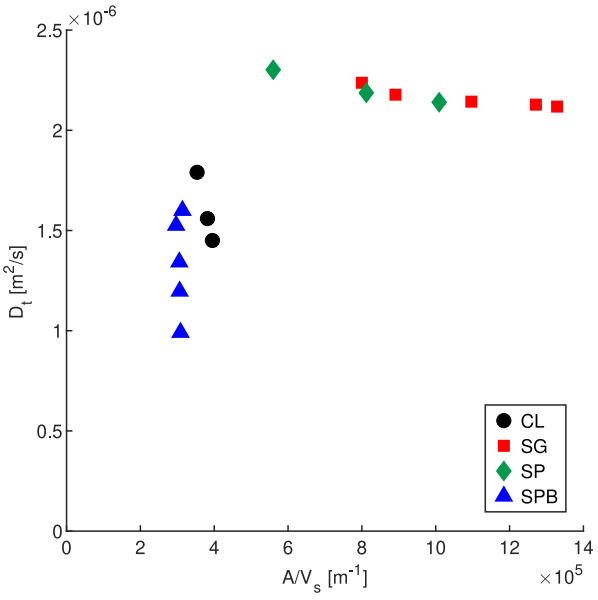

Fig. 10 – Thermal diffusivity D_t as a function of the surface area density A/V_s in m^{-1} for the different structures.

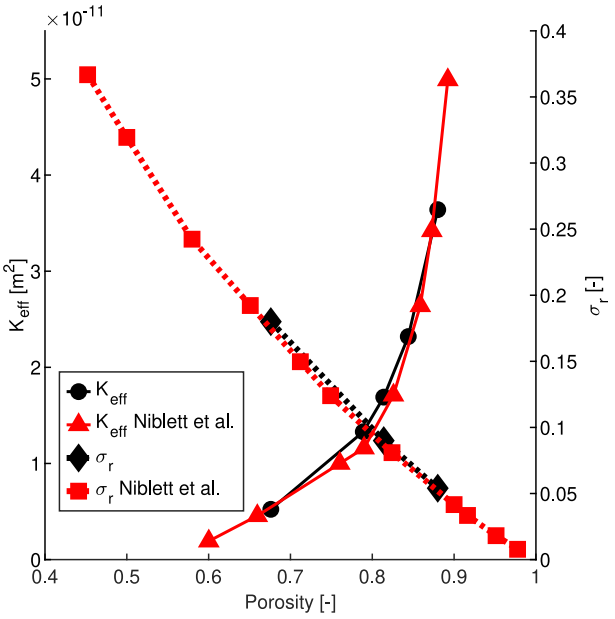

Fig. 12 – Comparison of the permeability K_{eff} in m^2 and the electrical conductivity ratio σ_r as a function of the porosity ϵ of the CL structures with the results of Niblett et al. [14].

$\rho_b \to 1$. This limit should hold since the structures only consist of solid volume when ρ_l/ρ_b approaches one and hence, the effective conductivity should approach the bulk value. However, as noted previously, a practical bound for the minimum porosity (and correspondingly the maximum ρ_l/ρ_b) is given by permeability requirements so that these upper limits on the validity of the Gibson-Ashby fits are not deemed critical to fluid transport layer applications.

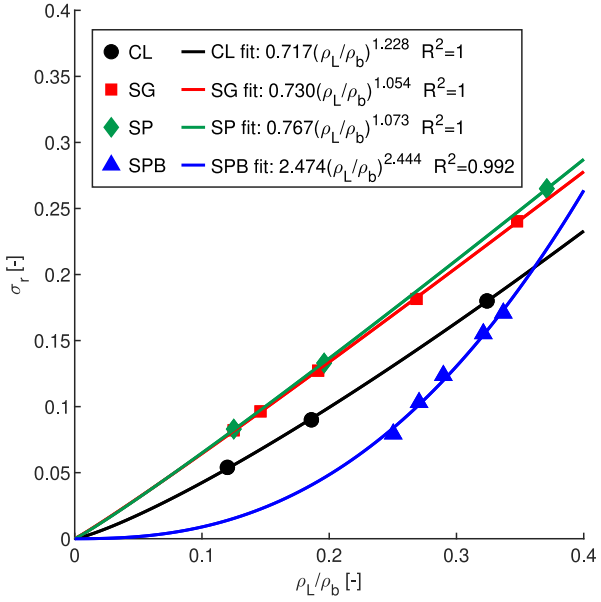

Fig. 11 – Gibson-Ashby relation applied to the electrical conductivity ratio σ_r for the different structures, including curve fit data.

It should be noted that the suitability of the Gibson-Ashby model to describe the conductivity ratio within the discussed bounds is partially due to the rather weak dependency of the corresponding electrical/thermal tortuosity on the porosity for the studied structures, see Fig. 7. Moreover, for the beam type CL and SPB structures the surface area density is virtually independent of the porosity, see Fig. 3, so that only the porosity remains as the decisive geometrical factor (besides the critical strut diameter for connectivity of the lattice that was discussed above). On the other hand, the nonlinear relationship between the surface area density and the porosity for the SG and SP walled structures shown in Fig. 3 can be accounted for in the fitting of the Gibson-Ashby model due to the similar characteristic of the respective exponential/power law dependencies. Overall, this reasoning supports the observed suitability of the Gibson-Ashby model to describe the conductivity ratios in the analyzed structures.

4.5. *Comparison to literature*

Comparisons with the work of Niblett et al. [14] are made as a way of verifying our simulation results. In particular, we consider the CL structures for this, as only they were modeled similarly in [14].

Fig. 12 shows this comparison for both the effective permeability and the conductivity ratio at varying porosity. A good agreement of our results with those of Niblett et al. [14] is seen. If the permeability is converted to a dimensionless number by dividing it by the squared unit cell size a^2 (see Table 2), the results are furthermore in the same order of magnitude as presented by Jung et al. [2]. According to the work of Jung et al. [2], the SP geometry moreover exhibits a larger permeability than the SG geometry, which is also seen in Fig. 2.

4.6. *Generality of our setup and results*

The results of this study are limited to specific unit cell sizes and porosities. They carry over to larger structures, however, due to the normalization of the computed properties, i.e. the permeability and (both electrical and thermal) conductivity ratios are independent of the structures' spatial extent but governed by limiting values of the applicable porosities. It should be noted that the computed values are only valid for cases where the flow or the conduction phenomena are occurring along the main axes (as considered in this work). This is because of the cubic anisotropy of the TPMS structures. If, for example, fluid permeation or current/heat conduction is desired in a diagonal direction, the structures' effective properties will change and further simulations are required for such cases.

5. Conclusions

The effective permeabilities and electrical/thermal conductivity ratios of three TPMS structures with porosities between 63% and 88% are computed and compared to corresponding values of a simple cubic lattice of similar dimensions. To this end, a computational workflow that enables an effective analysis of these porous structures is established and laid out in detail.

In general, the beam and the walled TPMS structures behave quite differently in terms of the variation of their effective parameters with porosity. Specifically, the following observations have been made.

- The attainable permeabilities for the beam TPMS and CL structures are up to one order of magnitude larger than for the walled TPMS structures.
- All structures' permeabilities exhibit an exponential dependency on porosity.
- The electrical current and heat conduction analysis reveal the superior conductivity ratios of the SG and SP structures compared to the CL and SPB ones, with the former two structures achieving on average 1.3 and 2.6 times higher values and the SPB structure performing worst, overall.
- The results indicate that the walled TPMS structures' conductive properties are mainly depended on porosity and surface area density. For the beam type TPMS and CL structures, these properties depended solely on the porosity and in the high-porosity limit also on the minimal strut diameters.
- It is shown that the Gibson-Ashby relationship is an adequate model for the electrical and thermal conductivities.

We hope for this work to serve as a useful guideline for functional property tuning of TPMS based porous media to achieve a desirable balance between thermal and electrical conductivity as well as permeability. Since there exists a large database on the mechanical properties of these structures, we believe that this study may complement these to assist the holistic design of these structures.

Credit authorship statement

Marco Sauermoser-Yri: Data curation, Formal analysis, Methodology, Software, Investigation, Visualization, Validation, Writing - original draft **Naresh Veldurthi:** Writing - original draft, Validation, editing & review **Christoph Hubertus Wölfle:** Data curation, Validation, Writing - review & editing **Preben Johnsen Svartvatn:** Conceptualization, Data curation, Formal analysis, Visualization, Methodology, Software, Investigation **Svenn Ove Flo Hoem:** Conceptualization, Data curation, Formal analysis, Visualization, Methodology, Software, Investigation **Markus Joakim Lid:** Conceptualization, Writing - review & editing **Robert Bock:** Supervision, Project administration, Validation, Writing - review & editing **James Palko:** Supervision, Conceptualization, Writing - review & editing **Jan Torgersen:** Supervision, Project administration, Resources, Funding acquisition, Validation, Writing - review & editing.

Data availability statement

The raw data required to reproduce these findings cannot be shared at this time due to technical or time limitations. The processed data required to reproduce these findings is available to download from https://doi.org/10.5281/zenodo.6491153.

Declaration of Competing Interest

The authors declare that they have no known competing financial interests or personal relationships that could have appeared to influence the work reported in this paper.

Acknowledgements

The results presented are part of a project that has received funding from the European Research Council (ERC) under the European Union's Horizon 2020 research and innovation program (Grant agreement No. 949807) with starting date May 2021. This project has received funding from the EXCELLENCE- Future Emerging Technologies (FET-OPEN) framework of the European Union's Horizon 2020 research and innovation program (Grant Agreement no: 964955). The simulations were conducted on the IDUN computing infrastructure of the Norwegian University of Science and Technology (NTNU). The authors are grateful to Alberto Lorenzon for his support and the helpful discussions during the creation of the simulations.

Appendix A. Curve fit parameters

Table 5 gives a summary over all the presented curve fits for the various structures.

Appendix B. Supplementary material

The following are the supplementary data to this article:

Table 5 – Summary of all presented curve fits for the four different structures.

Structure	Parameter	$K_{eff} = ae^{b\epsilon}$	$A/V_s = ae^{b\epsilon} + c$	$\sigma_r = a\epsilon + b$	$k_r = ae^{bA/V_s}$	$\sigma_r = a\left(\frac{\rho_l}{\rho_b}\right)^b$
CL	a	2.26e-15	187	−0.623	2.50e3	0.717
	b	10.990	6.490	0.600	2.73e-5	1.228
	c	–	340,642	–	–	–
SG	a	6.80e-15	2931	−0.709	1.133	0.730
	b	7.420	6.307	0.702	−1.98e-6	1.054
	c	–	612,097	–	–	–
SP	a	1.96e-15	4412	−0.743	1.163	0.767
	b	9.220	5.615	0.732	−2.65e-6	1.073
	c	–	408,983	–	–	–
SPB	a	2.19e-14	2659	−1.051	3.47e17	2.474
	b	8.500	3.852	0.868	−1.39e-4	2.444
	c	–	261,977	–	–	–

Appendix A. Supplementary data

Supplementary data to this article can be found online at https://doi.org/10.1016/j.jmrt.2023.09.242.

REFERENCES

[1] Han L, Che S. An overview of materials with triply periodic minimal surfaces and related geometry: from biological structures to self-assembled systems. Adv Mater 2018;30(17):1–22. https://doi.org/10.1002/adma.201705708.

[2] Jung Y, Torquato S. Fluid permeabilities of triply periodic minimal surfaces. Phys Rev E - Stat Nonlinear Soft Matter Phys 2005;72(5):1–8. https://doi.org/10.1103/PhysRevE.72.056319. arXiv:0603394.

[3] Tran P, Peng C. Triply periodic minimal surfaces sandwich structures subjected to shock impact, Jnl of Sandwich. Struct. Mater. 2021;23:2146–75. https://doi.org/10.1177/1099636220905551.

[4] Emanuelli L, Biasi RD, Plessis AD, Lora C, Jam A, Benedetti M, et al. Metrological characterization of porosity graded β-Ti21S triply periodic minimal surface cellular structure manufactured by laser powder bed fusion. Int J Bioprint 2023;9(4):729. https://doi.org/10.18063/ijb.729.

[5] Maskery I, Sturm L, Aremu AO, Panesar A, Williams CB, Tuck CJ, et al. Insights into the mechanical properties of several triply periodic minimal surface lattice structures made by polymer additive manufacturing. Polymer 2018;152:62–71. https://doi.org/10.1016/j.polymer.2017.11.049.

[6] Al-Ketan O, Lee DW, Rowshan R, Abu Al-Rub RK. Functionally graded and multi-morphology sheet TPMS lattices: design, manufacturing, and mechanical properties. J Mech Behav Biomed Mater 2020;102:103520. https://doi.org/10.1016/j.jmbbm.2019.103520. August 2019.

[7] Lu J, Dong P, Zhao Y, Zhao Y, Zeng Y. 3D printing of TPMS structural ZnO ceramics with good mechanical properties. Ceram Int 2021;47(9):12897–905. https://doi.org/10.1016/j.ceramint.2021.01.152.

[8] S. Ma, Q. Tang, X. Han, Q. Feng, J. Song, R. Setchi, et al, Manufacturability, mechanical properties, mass-transport properties and biocompatibility of triply periodic minimal surface (TPMS) porous scaffolds fabricated by selective laser melting, Mater Des 2020;195. https://doi.org/10.1016/j.matdes.2020.109034.

[9] Cai Z, Liu Z, Hu X, Kuang H, Zhai J. The effect of porosity on the mechanical properties of 3D-printed triply periodic minimal surface (TPMS) bioscaffold. Bio-Design and Manuf. 2019;2(4):242–55. https://doi.org/10.1007/s42242-019-00054-7.

[10] du Plessis A, Yadroitsava I, Yadroitsev I, le Roux SG, Blaine DC. Numerical comparison of lattice unit cell designs for medical implants by additive manufacturing. Virtual Phys Prototyp 2018;13(4):266–81. https://doi.org/10.1080/17452759.2018.1491713.

[11] Cheng Z, Li X, Xu R, Jiang P. Investigations on porous media customized by triply periodic minimal surface: heat transfer correlations and strength performance. Int Commun Heat Mass Tran 2021;129:105713. https://doi.org/10.1016/j.icheatmasstransfer.2021.105713.

[12] Qureshi ZA, Al-Omari SAB, Elnajjar E, Al-Ketan O, Al-Rub RA. Using triply periodic minimal surfaces (TPMS)-based metal foams structures as skeleton for metal-foam-PCM composites for thermal energy storage and energy management applications. Int Commun Heat Mass Tran 2021;124(April):105265. https://doi.org/10.1016/j.icheatmasstransfer.2021.105265.

[13] Catchpole-Smith S, Sélo RRJ, Davis AW, Ashcroft IA, Tuck CJ, Clare A. Thermal conductivity of TPMS lattice structures manufactured via laser powder bed fusion. Addit Manuf 2019;30(August):100846. https://doi.org/10.1016/j.addma.2019.100846.

[14] Niblett D, Niasar V, Holmes S. Enhancing the performance of fuel cell gas diffusion layers using ordered microstructural design. J Electrochem Soc 2020;167(1):013520. https://doi.org/10.1149/2.0202001jes.

[15] W. Li, G. Yu, Z. Yu, Bioinspired heat exchangers based on triply periodic minimal surfaces for supercritical co2 cycles, Appl Therm Eng.179. doi:https://doi.org/10.1016/j.applthermaleng.2020.115686.

[16] Torquato S, Haslach Jr HW. Random heterogeneous materials: microstructure and macroscopic properties. Appl Mech Rev 2002;55(4):B62–3. https://doi.org/10.1115/1.1483342.

[17] Torquato S, Donev A. Minimal surfaces and multifunctionality. Proceedings of the Royal Society of London. Series A: Math Phys Eng Sci 2004;460:1849–56. https://doi.org/10.1098/rspa.2003.1269.

[18] Ghanbarian B, Hunt AG, Ewing RP, Sahimi M. Tortuosity in porous media: a critical review. Soil Sci Soc Am J 2013;77(5):1461–77. https://doi.org/10.2136/sssaj2012.0435.

[19] W. Sobieski, M. Matyka, J. Gołembiewski, S. Lipiński, The Path Tracking Method as an alternative for tortuosity determination in granular beds, Granul Matter 2018;20 (4). https://dot.org/10.1007/s10035-018-0842-x.

[20] Jia H, Lei H, Wang P, Meng J, Li C, Zhou H, et al. An experimental and numerical investigation of compressive response of designed Schwarz Primitive triply periodic

minimal surface with non-uniform shell thickness. Extreme Mechanics Letters 2020;37:100671. https://doi.org/10.1016/j.eml.2020.100671.
[21] Feng J, Liu B, Lin Z, Fu J. Isotropic porous structure design methods based on triply periodic minimal surfaces. Mater Des 2021;210:110050. https://doi.org/10.1016/j.matdes.2021.110050.
[22] ANSYS®. ANSYS® spaceclaim 2021 R1 user's guide. 2021. https://ansyshelp.ansys.com/account/secured?returnurl=/Views/Secured/corp/v211/en/spaceclaim/index.html. [Accessed 21 February 2022].
[23] ANSYS®. ANSYS® fluent 2021 R1 user's guide. 2021. https://ansyshelp.ansys.com/account/secured?returnurl=/Views/Secured/corp/v211/en/flu_ug/flu_ug.html. [Accessed 21 February 2022].
[24] Childs EC, Collis-George N, Taylor GI. The permeability of porous materials. Proc Roy Soc Lond Math Phys Sci 1950;201(1066):392–405. https://doi.org/10.1098/rspa.1950.0068.
[25] Day MA. The No-slip condition of fluid dynamics. Erkenntnis (1975-) 1990;33(3):285–96. http://www.jstor.org/stable/20012308.
[26] Squires TM, Quake SR. Microfluidics: fluid physics at the nanoliter scale. Rev Mod Phys 2005;77(3):977–1026. https://link.aps.org/doi/10.1103/RevModPhys.77.977.
[27] S. Sharma, Glassy Carbon: a promising material for micro and nanomanufacturing, Materials 2018;11 (10). https://doi.org/10.3390/ma11101857.
[28] Goodfellow. Supplier data - vitreous carbon (goodfellow). 2022. https://www.azom.com/article.aspx?ArticleID=1838. [Accessed 21 February 2022].
[29] Takahasi Y, Westrum J, Edgar F. Glassy carbon low-temperature thermodynamic properties. J Chem Thermodyn 1970;2:847–54. https://doi.org/10.1002/9780470145333.ch113.
[30] T. Yamada, R. Matsuzaki, Evaluation of permeability applicability based on continuum mechanics law in fluid flow through graphene membrane, Sci Rep 9. https://doi.org/10.1038/s41598-019-49131-y.
[31] Al-Ketan O, Rowshan R, Abu Al-Rub RK. Topology-mechanical property relationship of 3D printed strut, skeletal, and sheet based periodic metallic cellular materials. Addit Manuf 2018;19:167–83. https://doi.org/10.1016/j.addma.2017.12.006.
[32] Guerreiro R, Pires T, Guedes JM, Fernandes PR, Castro APG. On the tortuosity of TPMS scaffolds for tissue engineering. Symmetry 2020;12(4):17–9. https://doi.org/10.3390/SYM12040596.
[33] Kaur I, Singh P. Flow and thermal transport characteristics of Triply-Periodic Minimal Surface (TPMS)-based gyroid and Schwarz-P cellular materials. Numer Heat Tran Part A: Applications 2021;79(8):553–69. https://doi.org/10.1080/10407782.2021.1872260.
[34] Gibson LJ, Ashby MF. Cellular solids: structure and properties. In: Cambridge solid state science series. 2nd ed. Cambridge University Press; 1997. https://doi.org/10.1017/CBO9781139878326.